ACS OMEGA

http://pubs.acs.org/journal/acsodf

Article

Effect of Porosity in Activated Carbon Supports for Silicon-Based Lithium-Ion Batteries (LIBs)

Yun Jeong Choi,[‖] Jeong Bin Choi,[‖] Ji Sun Im,* and Ji Hong Kim*

Cite This: *ACS Omega* 2023, 8, 19772−19780

Read Online

ACCESS | Metrics & More | Article Recommendations | Supporting Information

ABSTRACT: Activated carbon supports for Si deposition with different porosities were prepared, and the effect of porosity on the electrochemical characteristics was investigated. The porosity of the support is a key parameter affecting the Si deposition mechanism and the stability of the electrode. In the Si deposition mechanism, as the porosity of activated carbon increases, the effect of particle size reduction due to the uniform dispersion of Si was confirmed. This implies that the porosity of activated carbon can affect the rate performance. However, excessively high porosity reduced the contact area between Si and activated carbon, resulting in poor electrode stability. Therefore, controlling the porosity of activated carbon is essential to improving the electrochemical characteristics.

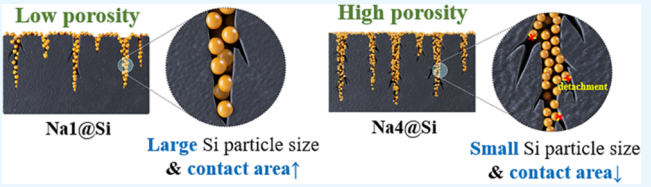

INTRODUCTION

Lithium-ion batteries (LIBs) are promising rechargeable energy storage technologies extensively used in various electronic devices owing to their high energy density, long cycle life, high working voltage, and maintenance costs.[1−4] As an anode material for commercial LIBs, graphite is widely used because of its low irreversible capacity and high cycle stability.[5,6] However, the theoretical capacity of graphite is limited to a relatively low 372 mAh/g, which does not meet the requirement for large-scale energy storage systems, such as the electric vehicle market.[5,7,8] Therefore, research on developing a new anode material to overcome the capacity limit is continuously progressing. Si is considered an alternative anode material to graphite because of its high theoretical capacity (4200 mAh/g) and low working potential lower than 0.5 V (vs Li+/Li).[9,10] However, particle pulverization occurs in the Si anode because of high volume expansion of more than 300% during repetitive charge−discharge processes. Consequently, an unstable and thick solid electrolyte interface (SEI) layer is continuously formed, leading to a reduction in Coulombic efficiency and stability degradation.[11−14] This problem can be improved by coating the surface of Si particles with a carbon matrix in the preparation of Si/carbon (Si@C) composites.[15−18] In general, the Si anode for LIBs is synthesized through two main methods, namely, bottom-up and top-down methods.[19−21] The top-down method utilizes bulk silicon or silica as the precursor, followed by various processes to obtain smaller-sized silicon particles.[22] The bottom-up method is an atomic- and molecular-scale self-assembly method, in which gaseous precursors (e.g., SiH_4) are decomposed to grow silicon particles on the substrate (template) or support.[23−25] This chemical vapor deposition (CVD) process is a simple and rapid method to achieve uniform surface coating and homogeneous growth of the Si particle on a substrate or support material.[26,27] Among the candidates that can be used as support, activated carbon is considered a promising material. Activated carbon can be produced from low-cost raw materials such as petroleum residue, steel byproducts, and biomass; it has excellent economic efficiency, and its manufacturing process is simple.[28−32] In addition, owing to its high porosity, activated carbon is expected to improve the site for Si particle deposition, and its porosity can be easily controlled by activation process parameters.[30,33] Although many studies[24,34−37] using porous carbon materials for Si deposition have been conducted, few studies have focused on the correlation between the porosity of activated carbon support and the Si deposition mechanism. In addition, a study on the effect of "porosity" on the electrochemical characteristics of the Si@C composite electrode is important. Therefore, in this study, activated carbon with different porosities was prepared using petroleum residue, and the electrochemical characteristics of each sample were investigated.

RESULTS AND DISCUSSION

Properties of Activated Carbon. To investigate the effect of NaOH during pitch activation, the field-emission scanning electron microscopy (FE-SEM) images of Na*x* samples were observed (Figure 1). The sample carbonized without NaOH showed a nonporous surface (Figure 1a). By contrast, slit-type

Received: March 6, 2023
Accepted: May 9, 2023
Published: May 23, 2023

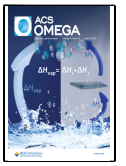

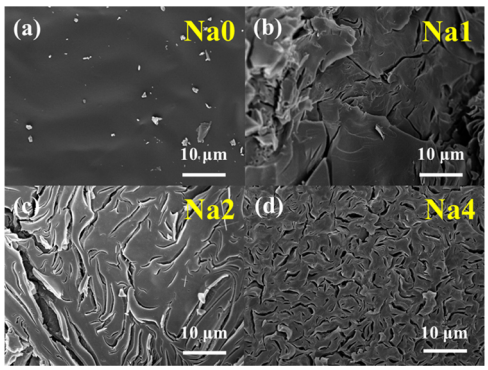

Figure 1. Field-emission scanning electron microscopy (FE-SEM) images of (a) the direct carbonization sample without NaOH and (b–d), activated carbons.

voids were commonly observed on the surface of the NaOH-added samples, indicating a porous surface (Figure 1b–d). The void fraction on the surface was quantified from the FE-SEM image, which was processed by binary thresholding (Figure S1). The calculated values were 9.43% (Na1), 10.59% (Na2), and 18.27% (Na3), indicating that the area occupied by voids increased with the addition of NaOH. In general, pitch coking occurs above 450 °C,[38,39] and NaOH decomposes above 500 °C.[40] Therefore, when the pitch is activated with NaOH as an agent (850 °C), activation by NaOH proceeds following the coke orientation. In this process, because etching occurs from the edge site with relatively high reactivity, a slit-type void is formed. The micrometer-scale slits observed on the surface are referred to as "voids" in this work.

The pore structure was investigated by Ar adsorption–desorption isotherm at 87 K (Figure 2). The micro/mesopore

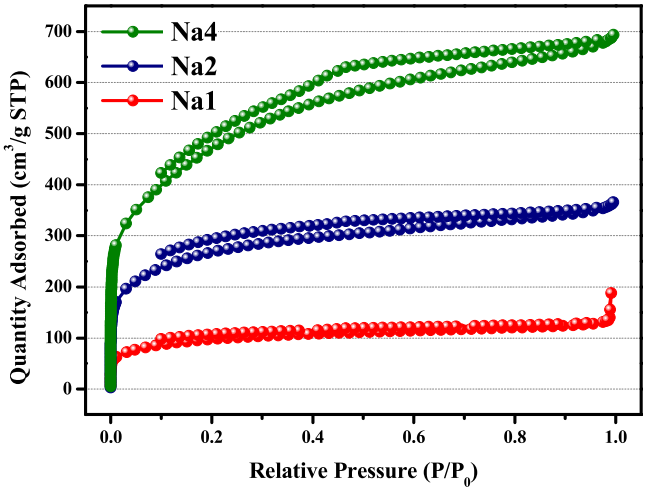

Figure 2. Ar adsorption–desorption isotherms of the activated carbons.

detected using the Brunauer–Emmett–Teller (BET) method is collectively referred to as "pore" in this work. "Porosity" is the result of reflecting "pores" and "voids". The adsorption–desorption isotherms of the samples show a hysteresis loop, which corresponds to type IV according to the IUPAC standard. The hysteresis shape in Figure 2 mainly appears in plate-type or slit-type mesopores,[41,42] which is consistent with the FE-SEM image. In particular, Na2 and Na4 show a sharp increase in the amount of Ar adsorbed at low relative pressure, indicating that these samples are relatively microporous materials. The specific surface area (SSA), total pore volume (V_{total}), micropore volume (V_{micro}), micropore fraction (M_f), and activation yield are summarized in Table 1. In Na4, the

Table 1. Characteristics of the Pore Structure of the Activated Carbons

sample	[a]SSA (m^2/g)	[b]V_{total} (cm^3/g)	[c]V_{micro} (cm^3/g)	[d]M_f (%)	[e]yield (%)
Na1	312.84	0.2404	0.1344	55.90	42.39
Na2	869.22	0.4682	0.3894	83.16	33.80
Na4	1513.76	0.8872	0.7472	84.22	13.17

[a]SSA: Specific surface area. [b]V_{total}: Total pore volume. [c]V_{micro}: Micropore volume. [d]M_f: Micropore fraction (micropore volume/total pore volume × 100). [e]Yield: Yield after activation.

Brunauer–Emmett–Teller SSA (S_{BET}) and V_{total} increased rapidly, corresponding to the increase in porosity due to the formation of micropores. The formed micropore and void improve the Li^+ storage capacity and can contribute to an increase in the specific capacity of the electrode.[43] In summary, the increased porosity by NaOH activation resulted from the simultaneous formation of nanometer-scale micro/mesopores and micrometer-scale slit voids. The next paragraph discusses how the Si particles are loaded on activated carbon according to their porosity in the SiH_4 CVD process.

Properties of Si@C Composites Prepared by the SiH_4/CH_4 CVD Method. The increased weight ratio after the SiH_4 and CH_4 CVD processes is shown in Figure 3a. Because of the higher porosity of the activated carbon, the loaded Si particles increased. However, considering that the specific surface area of Na4 (1514 m^2/g) increased by 5 times that of Na1 (313 m^2/g), the increase in the amount of loaded Si was negligible.; that is, the micro/mesopore possibly provided a minor contribution as a site for Si loading. To investigate the pore structure of Si-loaded activated carbon, Ar adsorption–desorption tests were conducted as shown in Figure 4. The SSAs of Na1 and Na2 were significantly reduced to 3.78 and 2.89 m^2/g (Table 2), respectively, indicating that most of the pores formed during the activation process were closed. By contrast, the SSA of Na4 remained relatively high, exceeding 100 m^2/g. According to the adsorption isotherms in Figure 4, the high SSA of Na4 is due to the presence of mesopores rather than micropores. As can be inferred from Figures 2 and 4 and Tables 1 and2, the Si particles are loaded, covering the pores rather than penetrating the pores. Compared to Na1 and Na2 samples, Na4 was relatively rich in pores; therefore, some pores that were not covered with Si remained. Owing to these remaining uncovered pores, Na4 showed a high initial capacity in subsequent electrochemical measurements (Table 3).

The layers of Si and coating carbon on activated carbon (Na2) are shown in the transmission electron microscopy (TEM) image of Figure 5. The Si layer loaded by SiH4 CVD had a thickness of approximately 5 nm (Figure 5a) and was composed of amorphous silicon (a-Si). In general, amorphous Si appears as two broad peaks centered at 28 and 52°.[44] Amorphous silicon was converted to crystalline Si after CH4 CVD at 900 °C (Figure 5b). Generally, amorphous Si is crystallized above 600 °C.[45] Moreover, a carbon-coating layer by CH4 CVD was observed. Similar results were confirmed in samples using Na1 and Na4 as supports.

https://doi.org/10.1021/acsomega.3c01506
ACS Omega 2023, 8, 19772–19780

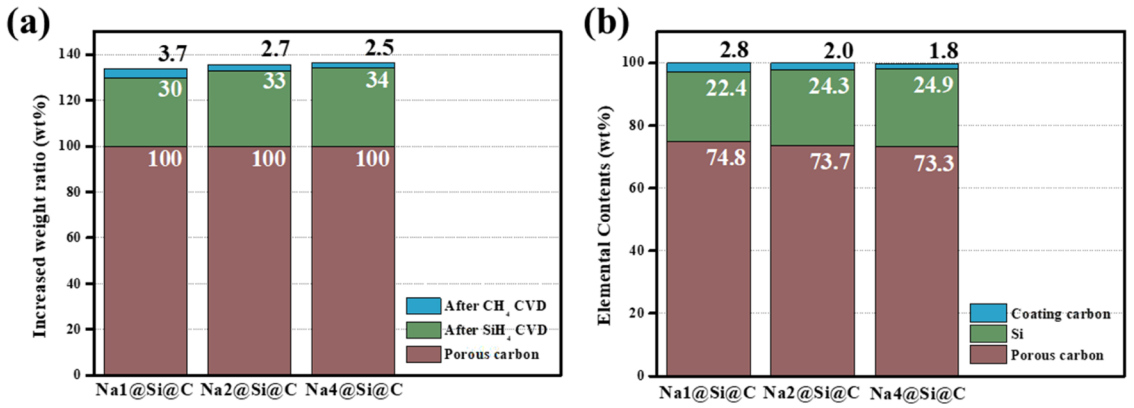

Figure 3. (a) Increased weight ratio of Nax@Si and Nax@Si@C after SiH_4 and CH_4 chemical vapor deposition (CVD). (b) Elemental contents of Nax@Si@C.

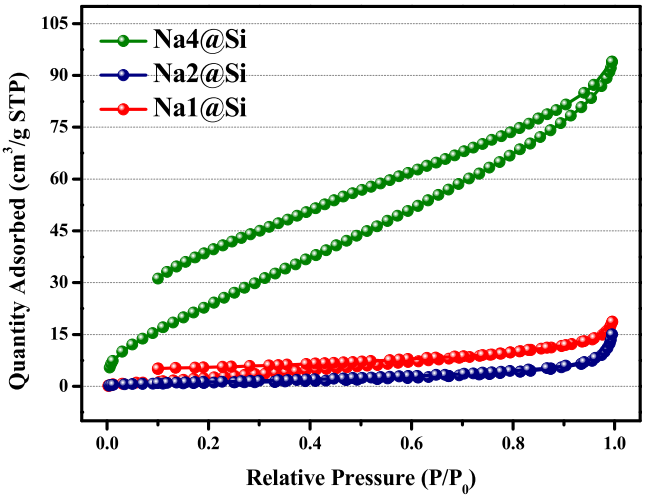

Figure 4. Ar adsorption−desorption isotherms of the Si-loaded activated carbons (Nax@Si).

Table 2. Characteristics of the Pore Structure after the SiH_4 CVD Process

sample	[a]SSA (m^2/g)	[b]V_{total} (cm^3/g)
Na1@Si	3.78	0.0239
Na2@Si	2.89	0.0192
Na4@Si	100.71	0.1202

[a]SSA: Specific surface area. [b]V_{total}: Total pore volume.

Table 3. Electrochemical Performance of the Prepared Nax@Si@C Composites

sample	1st charge capacity (mAh/g)	1st discharge capacity (mAh/g)	irreversible capacity (mAh/g)	initial Coulombic efficiency (%)
Na1@Si@C	984.22	935.53	48.69	95.05
Na2@Si@C	1134.04	1089.10	44.94	96.04
Na4@Si@C	1277.72	1158.55	119.17	90.67

The crystal characteristics of samples after SiH_4 and CH_4 CVD processes were confirmed by X-ray diffraction (XRD) analysis. After SiH_4 CVD at 500 °C, an amorphous Si peak appeared (Figure 6a).[46,47] However, sharp peaks appeared at 28° (111), 47° (220), and 52° (311) after CH_4 CVD at 900 °C, indicating conversion to crystalline Si,[45] which was consistent with the TEM image (Figure 5). The XRD peak of pure Si not composited with carbon is shown in the Supporting Information (Figure S2). The particle size of loaded Si was calculated using the Bragg−Scherrer equation based on the (111) peak. The size of the Si particles were 21.5, 17.8, and 13.7 nm for Na1@Si@C, Na2@Si@C, and Na4@Si@C, respectively. As the porosity increased, the Si particle size decreased.

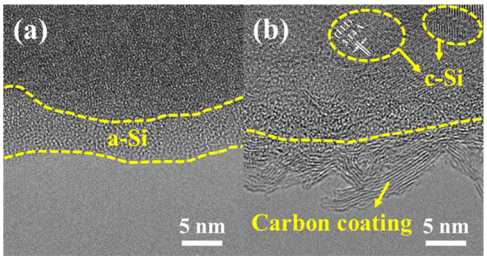

Figure 5. Transmission electron microscopy (TEM) images of (a) Na2@Si and (b) Na2@Si@C after SiH_4 and CH_4 CVD processes.

Figure 7 is a focused ion-beam scanning electron microscopy (FIB/SEM) image showing cross-sectional images of a sample milled by FIB. FIB-milled regions were imaged by back-scattered electrons (BSEs). This analysis is used to distinguish elements according to their brightness. The higher the atomic number, the higher the yield of BSE, resulting in brighter detection. This is because as the atomic number increases, the number of orbital electrons that interact with the beam electrons increases. Therefore, it is confirmed that Si (bright regions) was uniformly deposited in the void formed by NaOH. Consequently, the increase in porosity by voids was advantageous for uniformly dispersing Si particles.[48−50]

Electrochemical Performance of the Si@C Composite. The charge−discharge profiles of the first cycle of the Si@C composites electrode are shown in Figure 8, which is summarized in Table 3. For Si, a long lithiation plateau was observed below 0.1 V, which was related to the Li−Si alloying process to form Li_xSi compounds. Conversely, the delithiation plateau for dealloying was observed at 0.43 V.[51] As shown in Figure 8, a short delithiation plateau was additionally found at 0.09 V in addition to 0.43 V for the prepared samples. This plateau was attributed to lithium storage in the coating carbon layers and dealloying from the $Li_{22}Si_5$ alloy.[51−53] The discharge capacities of Na1@Si@C, Na2@Si@C, and Na4@Si@C were

https://doi.org/10.1021/acsomega.3c01506
ACS Omega 2023, 8, 19772−19780

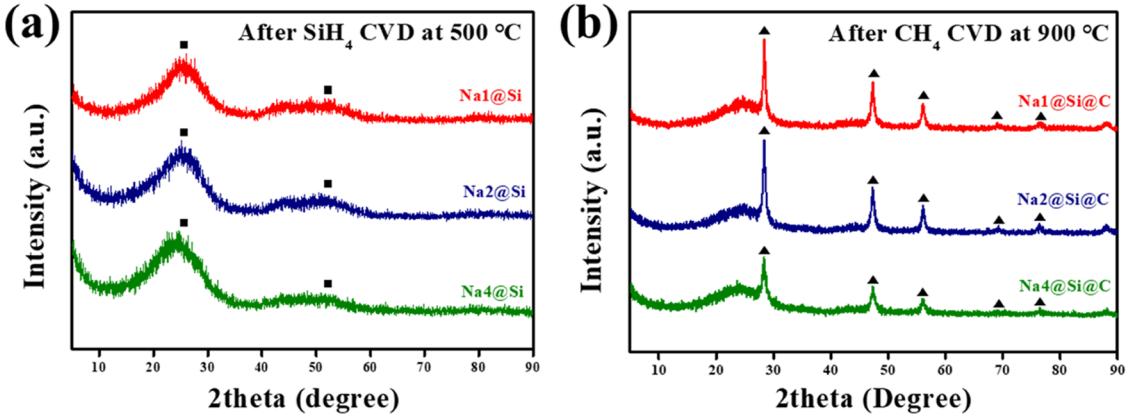

Figure 6. X-ray diffraction peaks after (a) SiH_4 and (b) CH_4 CVD processes.

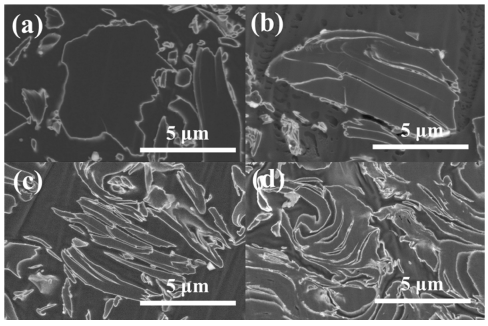

Figure 7. Back-scattered electron micrograph of FIB-milled cross section: (a) nonporous Na0@Si, (b) Na1@Si@C, (c) Na2@Si@C, and (d) Na4@Si@C after the SiH_4 CVD process.

initially 984, 1134, and 1278 mAh/g (Table 3), respectively, and increased with the porosity of activated carbon. The highest capacity of Na4@Si@C was attributed to the remaining micro/mesopores and voids providing active sites for Li^+ storage.[43] However, owing to the high specific surface area, the formation of the SEI layer by the electrolyte decomposition was promoted. Porous carbon with an enlarged specific surface area has more storage sites that could accommodate Li^+. This means that the active sites exposed to the electrolyte increase, and the formation of the SEI layer by the electrolyte decomposition is promoted in the first cycle.[54−56] Consequently, Na4@Si@C showed the highest irreversible discharge capacity (119.17 mAh/g) and poor initial Coulombic efficiency (90.67%). Excessively high specific surface area is a factor that promotes electrolyte decomposition, leading to the formation of a thick and unstable SEI layer. Therefore, a larger specific surface area directly leads to an increase in irreversible capacity and a decrease in initial Coulombic efficiency.[57−61]

The rate performance test of Si@C composite electrodes at scan rates of 0.1, 0.5, 1.0, and 2.0 are shown in Figure 9a. The cycle performance test was conducted at 0.05C for the first two cycles and then at 0.1C, as shown in Figure 9b. Na1@Si@C, which had the lowest porosity, showed the lowest capacity retention at 0.1−1C of current densities. Na1@Si@C was loaded with the largest Si particle size because of its low void fraction, as explained in the XRD data in Figure 6. The larger the particle size, the higher the charge-transfer resistance (R_{ct}) to Li^+, resulting in poor rate performance.[62−66] However, Na1@Si@C showed the least capacity fading after 50 cycles, indicating the highest cycle stability at 0.1C. The specific capacities of Na1@Si@C, Na2@Si@C, and Na4@Si@C after 50 cycles were 441, 326, and 214 mAh/g, respectively. Na1@Si@C had the lowest micro/mesopore fraction along with the void; thus, its contact area between the loaded Si particles and activated carbon is relatively large compared to those of Na2@Si@C and Na4@Si@C. Therefore, because the adhesion between the Si particles and the activated carbon is more robust, the Si particles can be less detached during cycling. The result of achieving such structural stability improvement is shown in Figure 12. Na2@Si@C exhibits the highest capacity retention at current densities of 0.1−1C, which was attributed to the size effect of Si particles. Meanwhile, despite having the smallest Si particle size, Na4@Si@C showed inferior rate performance to Na2@Si@C because of structural stability. Because Na4@Si@C is the most microporous sample, many uncontacted sites existed between the loaded Si particles and activated carbon when Si is loaded covering the pores. Therefore, structural deterioration due to the detachment of the Si particles proceeded rapidly. In addition, the content of the carbon-coating layer of Na4@Si@C was 1.8 wt %, which was the thinnest among those of the composites (Figure 3b); therefore, this should also be considered when comparing rate performance.

At a current density of 2C, Na1@Si@C had the highest capacity retention. However, this result does not explain why Na1@Si@C showed the highest rate performance at high current density. This outcome is due to the rapid deterioration of the electrochemical characteristics of Na2@Si@C and Na4@Si@C from 15 cycles when the 2C region started, as shown in Figure 9b.

To confirm the above differences in electrochemical characteristics of the prepared Si@C composites, electrical impedance spectroscopy (EIS) measurements were conducted. Figure 10 shows the Nyquist curves of electrodes after five cycles by EIS measurement, and the equivalent circuit is inserted. R_b corresponds to the bulk resistance, which mainly reflects the sum of ohmic resistances. R_{SEI} corresponds to resistance due to the SEI layer formation, and R_{ct} corresponds to charge-transfer resistance at the interface between the electrode and the electrolyte.[67] Na1@Si@C, which has the largest Si particle size, has the highest R_{SEI} because particle pulverization and subsequent formation of a new SEI layer on the pulverized Si fragments are actively promoted.[68] Moreover, the highest R_{ct} of 6.64 Ω was obtained, which was related to inferior rate performance. Meanwhile, Na2@Si@C had the lowest R_{ct} (4.08 Ω) and R_{SEI} (0.86 Ω), indicating superior

https://doi.org/10.1021/acsomega.3c01506
ACS Omega 2023, 8, 19772−19780

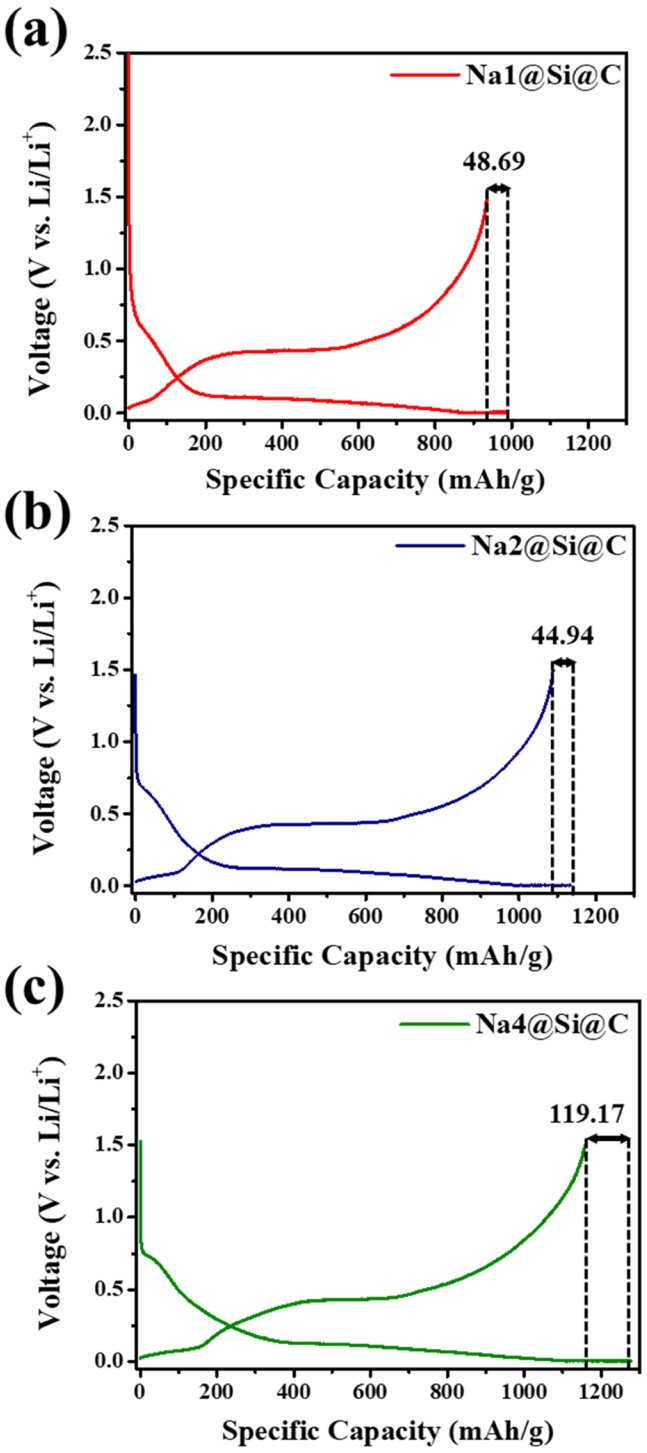

Figure 8. Voltage profiles of the Nax@Si@C composite electrodes for the first cycle at 0.05C: (a) Na1@Si@C, (b) Na2@Si@C, and (c) Na4@Si@C.

structural stability for the initial five cycles than that of Na4@Si@C.

To further investigate the electrochemical kinetics, the Li-ion diffusion coefficient (D_{Li}^+) was calculated. The Warburg factor (σ) was obtained using eq 1

$$Z' = R_1 + R_{ct} + \sigma\omega^{(-1/2)} \quad (1)$$

The value of σ was determined using the slope of linear fitting of the real part of impedance (Z') vs the inverse square root of angular frequency ($\omega^{-1/2}$), as shown in Figure 11.

D_{Li}^+ was calculated based on the obtained σ using eq 2

$$D_{Li^+} = \frac{R^2T^2}{2A^2n^2F^4C^2\sigma^2} \quad (2)$$

where R is the gas constant, T is the absolute temperature, A is the surface area of the electrode, F is the Faraday constant, and C is the molar concentration of Li^+ in the active material. Table 4 shows the D_{Li}^+ calculated according to the above equation. D_{Li}^+ was 6.3139×10^{-10} for Na1@Si@C and was significantly the smallest, which was related its poor rate performance and the highest R_{ct}. By contrast, the D_{Li}^+ of Na2@Si@C and Na4@Si@C, which have relatively small particle sizes, were 2.0394×10^{-9} and 2.1366×10^{-9}, respectively, which were significantly similar.

CONCLUSIONS

In this study, pitch-based activated carbon was prepared as support for Si loading, and then Si@C composite electrodes were prepared using the SiH_4 and CH_4 CVD processes. With an increasing ratio of NaOH, the activation agent, the slit-type voids on the micrometer scale and micro/mesopores on the nanometer scale simultaneously increased, resulting in improved porosity. In particular, Na4@Si@C, which was the most microporous composite, had the highest SSA of 1514 m^2/g. As the porosity increased, the size of loaded Si decreased, and the Si particle sizes of Na1@Si@C, Na2@Si@C, and Na4@Si@C were 21.5, 17.8, and 13.7 nm, respectively. This trend was attributed to an increase in the loading site by the void rather than by the micro/mesopore.

In the electrochemical tests, the void is a factor related to Si particle size, contributing to rate performance improvement. Meanwhile, micro/mesopore is a factor related to structural stability, which deteriorates the stability of the electrode. Consequently, Na2@Si@C exhibited the best rate performance within the range of 0.1−1.0C, while Na1@Si@C showed the highest stability during 50 cycles.

This study is meaningful because it presents a direction for optimizing the properties of activated carbon support for Si deposition. However, because Si CVD was conducted under atmospheric pressure, the diffusion effect into the micro/mesopores in the activated carbon was minimal. Nevertheless, the improvement of electrochemical characteristics by Si deposited in microscale voids was confirmed. Based on the above results, the stability and initial Coulombic efficiency of the electrode can be improved by inducing the diffusion of Si into the pores. In the future, we will solve the mentioned limitations through pressure control methods, such as vacuum pretreatment.

EXPERIMENTAL SECTION

Preparation of the Na@Si@C Composite Anode Material. *Preparation of Activated Carbon for SiH_4 CVD; Nax.* Petroleum-based pitch (softening point: 160 °C, Ansan Co.) was used as an activated carbon precursor. The activated carbon was prepared by chemical activation, in which NaOH (98.0%, Samchun Chemical Co., Ltd) was used as the activation agent. Before activation, the pitch and NaOH were uniformly pulverized (under 100 μm) and mixed. The weight ratio of pitch to NaOH was controlled from 1:1 to 1:4. The

https://doi.org/10.1021/acsomega.3c01506
ACS Omega 2023, 8, 19772−19780

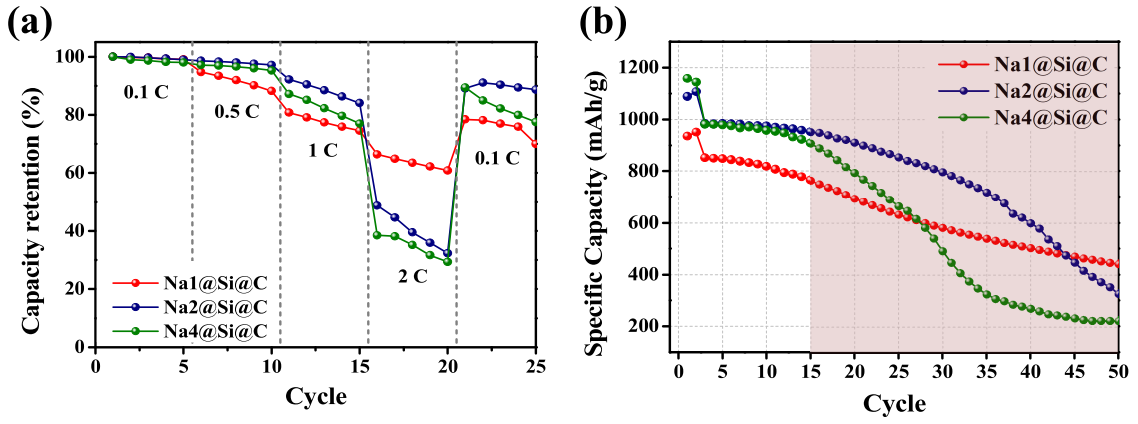

Figure 9. (a) Rate capability of the Nax@Si@C composite electrodes at different current densities and (b) the capacity of the Nax@Si@C composite electrodes at 0.05 and 0.1C after 50 cycles.

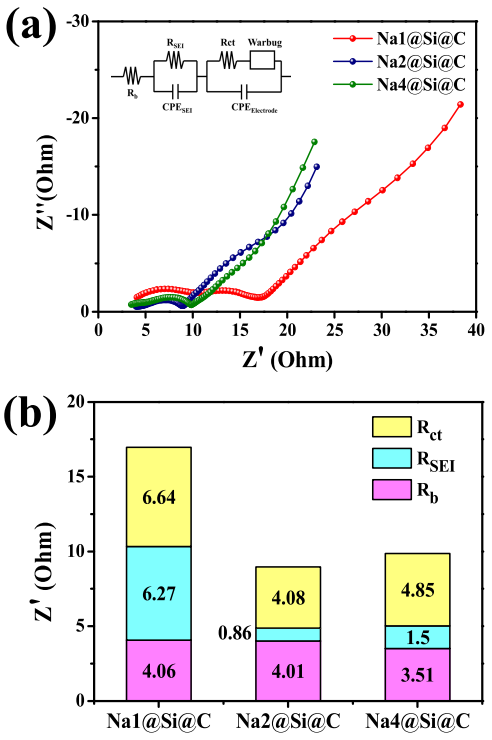

Figure 10. (a) Nyquist plot and (b) classified resistance of the electrode after five cycles.

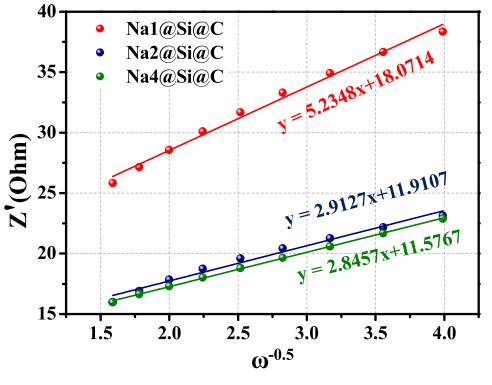

Figure 11. Relationship between imaginary resistance (Z') and the inverse square root of angular speed ($\omega^{-0.5}$) in the low-frequency region.

mixture was transferred to an alumina boat, which was placed into a horizontal stainless tube furnace. The activation was performed at 850 °C (5 °C/min) for 60 min under N_2 flow (100 cc/min). The samples obtained after activation were repeatedly washed with distilled water until a pH of 7 was reached to remove any soluble impurities. The washed samples were dried in an oven at 80 °C for 24 h. The samples were denoted by Nax (x = 0, 1, 2, and 4) according to the ratio of NaOH.

Preparation of Activated Carbon-Loaded Si; Nax@Si. To deposit Si particles on the activated carbon, CVD using SiH_4 was conducted. Here, 0.5 g of activated carbon was placed into a quartz-tube furnace. Then, the sample was heated to 500 °C under Ar flow. When the target temperature was reached, 30 cc/min of SiH_4 (9.99%, diluted H_2) was injected into the quartz-tube furnace and maintained for 60 min. After the reaction, the injection gas was converted to Ar flow, and then the furnace was cooled to room temperature. The samples were named Nax@Si.

Carbon Coating of Nax@Si by the CH_4 CVD Method; Nax@Si@C. To suppress the side reaction of the anode during the charge/discharge process, Nax@Si was coated with carbon as follows: 0.5 g of Nax@Si was heated to 900 °C under Ar flow. When the target temperature was reached, 100 cc/min of CH_4 (99.9%) was injected into the quartz-tube furnace and maintained for 30 min. After the reaction, the injection gas was converted to Ar flow, and then the furnace was cooled to room temperature. The samples were named Nax@Si@C. The increase in weight after the reaction compared to the initial weight was assumed to be the amount of Si and carbon coated.

Characterization. The surface roughness of activated carbon was confirmed by FE-SEM (TESCAN MIRA3 LMU) imaging. The micrometer-scale slits observed on the surface are referred to as "voids" in this work. The pore structures were measured by Ar adsorption−desorption at 87 K using ASAP 2420 (ASAP 2020, Micromeritics). The SSA was calculated using BET equations, and the micropore volume was calculated from the t-plot method. The micro/mesopores detected using the BET method are collectively referred to as "pores" in this work. "Porosity" is the result of reflecting pores and voids. The crystal structure of the loaded Si particle was analyzed by XRD (Rigaku Ultima IV) with Cu Kα (λ = 1.5418 Å) in the range of 5 < 2θ < 90°. The crystallite size was calculated using the Bragg−Scherrer equation based on the

https://doi.org/10.1021/acsomega.3c01506
ACS Omega 2023, 8, 19772−19780

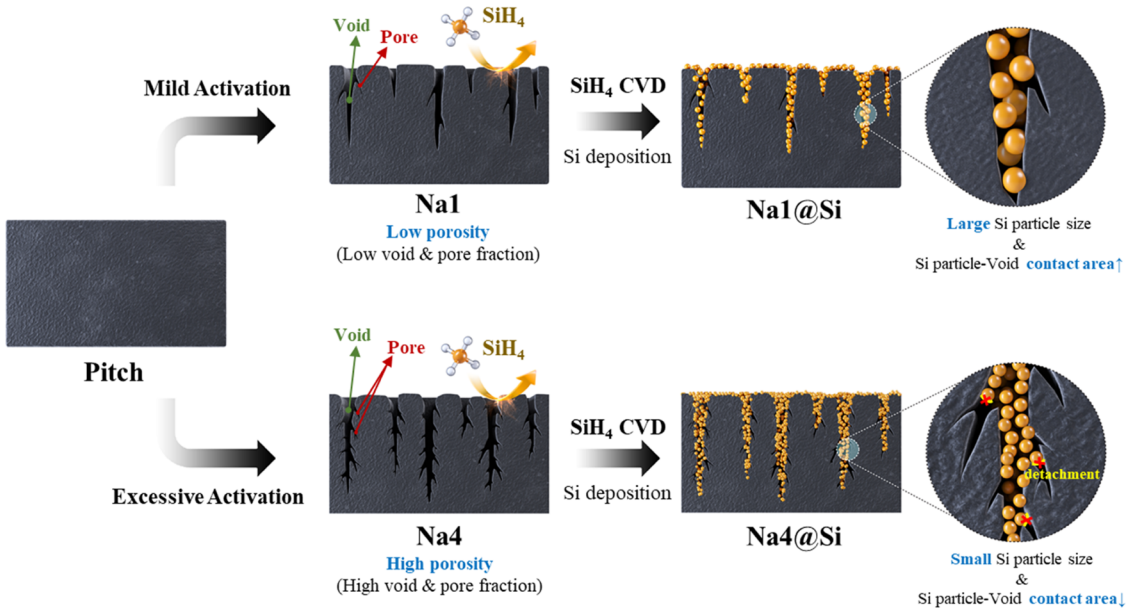

Figure 12. Schematic illustration of the preparation of the Nax@Si@C composite.

Table 4. Li-Ion Diffusion Coefficient of Prepared Nax@Si@C Composite Electrodes after Five Cycles

sample	Na1@Si@C	Na2@Si@C	Na4@Si@C
after five cycles	6.3139×10^{-10}	2.0394×10^{-9}	2.1366×10^{-9}

(111) peaks. TEM (FEI Talos) analysis was performed to confirm the loaded Si and carbon-coating layers.

Electrochemical Measurement. Electrochemical measurements were performed using coin-type cells (CR2032-type). For the electrode, the slurry was mixed with a composition of 90 wt % active material, 5 wt % Super P, 2.5 wt % carboxymethylcellulose, and 2.5 wt % styrene−butadiene rubber using a thinky mixer. The slurry was subsequently coated uniformly on a Cu current collector and dried at 80 °C for 8 h. The electrodes were pressed and then punched to a diameter of 13.5 mm. The coin cells were assembled in an Ar-filled glovebox (H_2O, O2 < 0.5 ppm). The electrolyte was 1.0 M $LiPF_6$ in a mixture of ethylene carbonate and diethyl carbonate (1:1 vol %). The galvanostatic charge−discharge of the cells was measured at 25 °C in a voltage range of 0.01−1.5 V vs Li/Li+ using an instrument (WBCS3000, Wonatech). The coin cells were lithiated at a rate of 0.1C and delithiated at various rates ranging from 0.1 to 2C to measure the rate performance. EIS measurements were conducted at the amplitude of 10 mV and a frequency range of 100 kHz to 0.01 Hz.

■ ASSOCIATED CONTENT

Supporting Information

The Supporting Information is available free of charge at https://pubs.acs.org/doi/10.1021/acsomega.3c01506.

Scanning electron microscopy image of the activated carbons for quantifying void fraction by binary thresholding; X-ray diffraction peaks of pure Si (PDF)

■ AUTHOR INFORMATION

Corresponding Authors

Ji Sun Im − *C1 Gas & Carbon Convergent Research, Korea Research Institute of Chemical Technology (KRICT), Daejeon 34114, Republic of Korea; Advanced Materials and Chemical Engineering, University of Science and Technology (UST), Daejeon 34113, Republic of Korea;* orcid.org/0000-0001-7724-9590; Email: jsim@krict.re.kr

Ji Hong Kim − *C1 Gas & Carbon Convergent Research, Korea Research Institute of Chemical Technology (KRICT), Daejeon 34114, Republic of Korea*; Email: pic10@krict.re.kr

Authors

Yun Jeong Choi − *C1 Gas & Carbon Convergent Research, Korea Research Institute of Chemical Technology (KRICT), Daejeon 34114, Republic of Korea; Department of Chemical Engineering and Applied Chemistry, Chungnam National University, Daejeon 34134, Republic of Korea*

Jeong Bin Choi − *C1 Gas & Carbon Convergent Research, Korea Research Institute of Chemical Technology (KRICT), Daejeon 34114, Republic of Korea*

Complete contact information is available at: https://pubs.acs.org/10.1021/acsomega.3c01506

Author Contributions

‖Y.J.C. and J.B.C. contributed equally to this work.

Notes

The authors declare no competing financial interest.

■ ACKNOWLEDGMENTS

The authors declare the following financial interests/personal relationships that may be considered as potential competing interests: This work was supported by the Technology Innovation Program (20010853, Development of natural gas based carbon material on graphite structure for high crystalline conductivity) funded By the Ministry of Trade, Industry & Energy (MOTIE, Korea).

https://doi.org/10.1021/acsomega.3c01506
ACS Omega 2023, 8, 19772−19780

REFERENCES

(1) You, S.; Tan, H.; Wei, L.; Tan, W.; Li, C. C. Design Strategies of Si/C Composite Anode for Lithium-Ion Batteries. *Chem. – Eur. J.* **2021**, *27*, 12237–12256.

(2) Chae, S.; Choi, S. H.; Kim, N.; Sung, J.; Cho, J. Integration of Graphite and Silicon Anodes for the Commercialization of High-Energy Lithium-Ion Batteries. *Angew. Chem., Int. Ed.* **2020**, *59*, 110–135.

(3) Nzereogu, P. U.; Omah, A. D.; Ezema, F. I.; Iwuoha, E. I.; Nwanya, A. C. Anode materials for lithium-ion batteries: A review. *Appl. Surf. Sci. Adv.* **2022**, *9*, No. 100233.

(4) Chang, H.; Wu, Y. R.; Han, X.; Yi, T. F. Recent developments in advanced anode materials for lithium-ion batteries. *Energy Mater.* **2021**, *1*, No. 100003.

(5) Natarajan, S.; Aravindan, V. An Urgent Call to Spent LIB Recycling: Whys and Wherefores for Graphite Recovery. *Adv. Energy Mater.* **2020**, *10*, No. 2002238.

(6) Wang, X.; Chen, J.; Dong, C.; Wang, D.; Mao, Z. Hard Carbon Derived from Graphite Anode by Mechanochemistry and the Enhanced Lithium-Ion Storage Performance. *ChemElectroChem* **2022**, *9*, No. e202101613.

(7) Ma, Z.; Cui, Y.; Xiao, X.; Deng, Y.; Song, X.; Zuo, X.; Nan, J. A reconstructed graphite-like carbon micro/nano-structure with higher capacity and comparative voltage plateau of graphite. *J. Mater. Chem. A* **2016**, *4*, 11462–11471.

(8) Zhao, L.; Ding, B.; Qin, X. Y.; Wang, Z.; Lv, W.; He, Y. B.; Yang, Q. H.; Kang, F. Revisiting the Roles of Natural Graphite in Ongoing Lithium-Ion Batteries. *Adv. Mater.* **2022**, *34*, No. 2106704.

(9) Yang, Y.; Yuan, W.; Kang, W.; Ye, Y.; Pan, Q.; Zhang, X.; Ke, Y.; Wang, C.; Qiu, Z.; Tang, Y. A review on silicon nanowire-based anodes for next-generation high-performance lithium-ion batteries from a material-based perspective. *Sustainable Energy Fuels* **2020**, *4*, 1577–1594.

(10) Zhang, Y.; Wu, B.; Mu, G.; Ma, C.; Mu, D.; Wu, F. Recent progress and perspectives on silicon anode: Synthesis and prelithiation for LIBs energy storage. *J. Energy Chem.* **2022**, *64*, 615–650.

(11) Ashuri, M.; He, Q.; Shaw, L. L. Silicon as a potential anode material for Li-ion batteries: where size, geometry and structure matter. *Nanoscale* **2016**, *8*, 74–103.

(12) Xu, Z. L.; Gang, Y.; Garakani, M. A.; Abouali, S.; Huang, J. Q.; Kim, K. J. Carbon-coated mesoporous silicon microsphere anodes with greatly reduced volume expansion. *J. Mater. Chem. A* **2016**, *4*, 6098–6106.

(13) Li, X.; Gu, M.; Hu, S.; Kennard, R.; Yan, P.; Chen, X.; Wang, C.; Sailor, M. J.; Zhang, J. G.; Liu, J. Mesoporous silicon sponge as an anti-pulverization structure for high-performance lithium-ion battery anodes. *Nat. Commun.* **2014**, *5*, No. 4105.

(14) Ma, J.; Sung, J.; Lee, Y.; Son, Y.; Chae, S.; Kim, N.; et al. Strategic Pore Architecture for Accommodating Volume Change from High Si Content in Lithium-Ion Battery Anodes. *Adv. Energy Mater.* **2020**, *10*, No. 1903400.

(15) Shen, X.; Tian, Z.; Fan, R.; Shao, L.; Zhang, D.; Cao, G.; Kou, L.; Bai, Y. Research progress on silicon/carbon composite anode materials for lithium-ion battery. *J. Energy Chem.* **2018**, *27*, 1067–1090.

(16) You, S.; Tan, H.; Wei, L.; Tan, W.; Li, C. C. Design Strategies of Si/C Composite Anode for Lithium-Ion Batteries. *Chem. – Eur. J.* **2021**, *27*, 12237–12256.

(17) Wang, F.; Chen, G.; Zhang, N.; Liu, X.; Ma, R. Engineering of carbon and other protective coating layers for stabilizing silicon anode materials. *Carbon Energy* **2019**, *1*, 219–245.

(18) Dou, F.; Shi, L.; Chen, G.; Zhang, D. Silicon/Carbon Composite Anode Materials for Lithium-Ion Batteries. *Electrochem. Energy Rev.* **2019**, *2*, 149–198.

(19) Zhang, L.; Al-Mamun, M.; Wang, L.; Dou, Y.; Qu, L.; Dou, S. X.; Liu, H. K.; Zhao, H. The typical structural evolution of silicon anode. *Cell Rep. Phys. Sci.* **2022**, *3*, No. 100811.

(20) Yuda, A. P.; Koraag, P. Y. E.; Iskandar, F.; Wasisto, H. S.; Sumboja, A. Advances of the top-down synthesis approach for high-performance silicon anodes in Li-ion batteries. *J. Mater. Chem. A* **2021**, *9*, 18906–18926.

(21) Su, X.; Wu, Q.; Li, J.; Xiao, X.; Lott, A.; Lu, W.; Sheldon, B. W.; Wu, J. Silicon-Based Nanomaterials for Lithium-Ion Batteries: A Review. *Adv. Energy Mater.* **2013**, *4*, No. 1300882.

(22) Park, Y.; Yoo, J.; Kang, M. H.; Kwon, W.; Joo, J. Photoluminescent and biodegradable porous silicon nanoparticles for biomedical imaging. *J. Mater. Chem. B* **2019**, *7*, 6271–6292.

(23) Cho, J. H.; Li, X.; Pictraux, S. T. The effect of metal silicide formation on silicon nanowire-based lithium-ion battery anode capacity. *J. Power Sources* **2012**, *205*, 467–473.

(24) Zhu, S.; Lin, Y.; Yan, Z.; Jiang, J.; Yang, D.; Du, N. Novel design of uniform Si@graphite@C composite as high-performance Li-ion battery anodes. *Electrochim. Acta* **2021**, *377*, No. 138092.

(25) Liu, H.; Liu, X.; Li, W.; Guo, X.; Wang, Y.; Wang, G.; Zhao, D. Porous Carbon Composites for Next Generation Rechargeable Lithium Batteries. *Adv. Energy Mater.* **2017**, *7*, No. 1700283.

(26) Xie, J.; Cao, G. S.; Zhao, X. B. Electrochemical performances of Si-coated MCMB as anode material in lithium-ion cells. *Mater. Chem. Phys.* **2004**, *88*, 295–299.

(27) Zhu, X.; Chen, H.; Wang, Y.; Xia, L.; Tan, Q.; Li, H.; Zhong, Z.; Su, F.; Zhao, X. S. Growth of silicon/carbon microrods on graphite microspheres as improved anodes for lithium-ion batteries. *J. Mater. Chem. A* **2013**, *1*, 4483–4489.

(28) Ioannidou, O.; Zabaniotou, A. Agricultural residues as precursors for activated carbon production-A review. *Renewable Sustainable Energy Rev.* **2007**, *11*, 1966–2005.

(29) Jang, E.; Choi, S. W.; Lee, K. B. Effect of carbonization temperature on the physical properties and CO2 adsorption behavior of petroleum coke-derived porous carbon. *Fuel* **2019**, *248*, 85–92.

(30) Seo, S. W.; Choi, Y. J.; Kim, J. H.; Cho, J. H.; Lee, Y. S.; Im, J. S. Micropore-structured activated carbon prepared by waste PET/petroleum-based pitch. *Carbon Lett.* **2019**, *29*, 385–392.

(31) Gayathiri, M.; Pulingam, T.; Lee, K. T.; Sudesh, K. Activated carbon from biomass waste precursors: Factors affecting production and adsorption mechanism. *Chemosphere* **2022**, *294*, No. 133764.

(32) Gao, Y.; Yue, Q.; Gao, B.; Li, A. Insight into activated carbon from different kinds of chemical activating agents: A review. *Sci. Total Environ.* **2020**, *746*, No. 141094.

(33) Kim, J. H.; Choi, Y. J.; Im, J. S.; Jo, A.; Lee, K. B.; Bai, B. C. Study of activation mechanism for dual model pore structured carbon based on effects of molecular weight of petroleum pitch. *J. Ind. Eng. Chem.* **2020**, *88*, 251–259.

(34) Peng, J.; Li, W.; Wu, Z.; Li, H.; Zeng, P.; Chen, G.; Chang, B.; Zhang, X.; Wang, X. Si/C composite embedded nano-Si in 3D porous carbon matrix and enwound by conductive CNTs as anode of lithium-ion batteries. *Sustainable Mater. Technol.* **2022**, *32*, No. e00410.

(35) You, S.; Tan, H.; Wei, L.; Tan, W.; Li, C. C. Design Strategies of Si/C Composite Anode for Lithium-Ion Batteries. *Chem. – A Eur. J.* **2021**, *27*, 12232–12446.

(36) Kim, B.; Ahn, J.; Oh, Y.; Tan, J.; Lee, D.; Lee, J. K.; Moon, J. Highly porous carbon-coated silicon nanoparticles with canyon-like surfaces as a high-performance anode material for Li-ion batteries. *J. Mater. Chem. A* **2018**, *6*, 3028–3037.

(37) Tian, W.; Zhang, H.; Duan, X.; Sun, H.; Shao, G.; Wang, S. Porous Carbons: Structure-Oriented Design and Versatile Applications. *Adv. Funct. Mater.* **2020**, *30*, No. 1909265.

(38) Han, Y. J.; Hwang, J. W.; Kim, K. S.; Kim, J. H.; Lee, J. D.; Im, J. S. Optimization of the preparation conditions for pitch based anode to enhance the electrochemical properties of LIBs. *J. Ind. Eng. Chem.* **2019**, *73*, 241–247.

(39) Yang, J. Y.; Kim, B. S.; Park, S. J.; Rhee, K. Y.; Seo, M. K. Preparation and characterization of mesophase formation of pyrolysis fuel oil-derived binder pitches for carbon composites. *Composites, Part B* **2019**, *165*, 467–472.

(40) Lillo-Ro'denas, M. A.; Cazorla-Amoro's, D.; Linares-Solano, A. Understanding chemical reactions between carbons and NaOH and

https://doi.org/10.1021/acsomega.3c01506
ACS Omega 2023, 8, 19772–19780

KOH An insight into the chemical activation mechanism. *Carbon* **2003**, *41*, 267−275.
(41) Wang, Z.; Cheng, Y.; Wang, G.; Ni, G.; Wang, L. Comparative analysis of pore structure parameters of coal by using low pressure argon and nitrogen adsorption. *Fuel* **2002**, *309*, No. 122120.
(42) Li, Y.; Li, C.; Qi, H.; Qi, H.; Yu, K.; Liang, Ce. Mesoporous activated carbon from corn stalk core for lithium ion batteries. *Chem. Phys.* **2018**, *506*, 10−16.
(43) Yang, X.; Wei, C.; Sun, C.; Li, X.; Chen, Y. High performance anode of lithium-ion batteries derived from an advanced carbonaceous porous network. *J. Alloys Compd.* **2017**, *693*, 777−781.
(44) Hatchard, T. D.; Dahn, J. R. *In Situ* XRD and Electrochemical Study of the Reaction of Lithium with Amorphous Silicon. *J. Electrochem. Soc.* **2004**, *151*, A838−A842.
(45) Westra, J. M.; Vavruková, V.; Šutta, P.; Van-Swaaij, R. A. C. M. M.; Zeman, M. Formation of thin-film crystalline silicon on glass observed by insitu XRD. *Energy Procedia* **2010**, *2*, 235−241.
(46) Devi Kumari, T. S.; Jeyakumar, D.; Kumar, T. P. Nano silicon carbide: a new lithium-insertion anode material on the horizon. *RSC Adv.* **2013**, *3*, No. 15028.
(47) Lee, J. K.; Smith, K. B.; Hayner, C. M.; Kung, H. H. Silicon nanoparticles−graphene paper composites for Li ion battery anodes. *Chem. Commun.* **2010**, *46*, 2025−2027.
(48) Fera, A.; He, Q.; Zhang, G.; Leapman, R. D. Quantitative method for estimating stain density in electron microscopy of conventionally prepared biological specimens. *J. Microsc.* **2020**, *277*, 71−78.
(49) Lešer, V.; Milani, M.; Tatti, F.; Tkalec, Z. P.; Štrus, J.; Drobne, D. Focused ion beam (FIB)/scanning electron microscopy (SEM) in tissue structural research. *Protoplasma* **2010**, *246*, 41−48.
(50) Kakubo, T.; Shimizu, K.; Kumagai, A.; Matsumoto, H.; Tsuchiya, M.; Amino, N.; Jinnai, H. Degradation of a Metal−Polymer Interface Observed by Element-Specific Focused Ion Beam-Scanning Electron Microscopy. *Langmuir* **2020**, *36*, 2816−2822.
(51) Shao, L.; Shu, J.; Wu, K.; Lin, X.; Li, P.; Shui, M.; Wang, D.; Long, N.; Ren, Y. Low pressure preparation of spherical Si@C@CNT@C anode material for lithium-ion batteries. *J. Electroanal. Chem.* **2014**, *727*, 8−12.
(52) Wang, C.; Niu, X.; Wang, D.; Zhang, W.; Shi, H.; Yu, L.; Wang, C.; Xiong, Z.; Ji, Z.; Yan, X.; Gu, Y. Simple preparation of Si/CNTs/C composite derived from photovoltaic waste silicon powder as high-performance anode material for Li-ion batteries. *Powder Technol.* **2022**, *408*, No. 117744.
(53) Epur, R.; Ramanathan, M.; Datta, M. K.; Hong, D. H.; Jampani, P. H.; Gattu, B.; Kumta, P. N. Scribable multi-walled carbon nanotube-silicon nanocomposites: a viable lithium-ion battery system. *Nanoscale* **2015**, *7*, 3504−3510.
(54) Tao, L.; Liu, L.; Chang, R.; He, H.; Zhao, P.; Liu, J. Structural and interface design of hierarchical porous carbon derived from soybeans as anode materials for potassium-ion batteries. *J. Power Source* **2020**, *463*, No. 228172.
(55) Wang, M. S.; Song, W. L.; Wang, J.; Fan, L. Z. Highly uniform silicon nanoparticle/porous carbon nanofiber hybrids towards free-standing high-performance anodes for lithium-ion batteries. *Carbon* **2015**, *82*, 337−345.
(56) Zhang, Q.; Xi, B.; Xiong, S.; Qian, Y. Carbon coated SiO nanoparticles embedded in hierarchical porous N-doped carbon nanosheets for enhanced lithium storage. *Inorg. Chem. Front.* **2021**, *8*, 4282−4290.
(57) Xu, Q.; Wang, Q.; Chen, D.; Zhong, Y.; Wu, Z.; Song, Y.; Wang, G.; Liu, Y.; Zhong, B.; Guo, X. Silicon/graphite composite anode with constrained swelling and a stable solid electrolyte interphase enabled by spent graphite. *Green Chem.* **2021**, *23*, 4531−4539.
(58) Shaker, M.; Ghazvini, A. A. S.; Riahifar, R.; Mumtaz, A. On the Relationship Between the Porosity and Initial Coulombic Efficiency of Porous Carbon Materials for the Anode in Lithium-Ion Batteries. *Electron. Mater. Lett.* **2022**, *18*, 400−406.
(59) Kim, K. H.; Cho, J. H.; Hwang, J. W.; Im, J. S.; Lee, Y. S. A key strategy to form a LiF-based SEI layer for a lithium-ion battery anode with enhanced cycling stability by introducing a semi-ionic Csingle bondF bond. *J. Ind. Eng. Chem.* **2021**, *99*, 48−54.
(60) Kim, J.; Chae, O. B.; Lucht, B. L. Perspective—Structure and Stability of the Solid Electrolyte Interphase on Silicon Anodes of Lithium-ion Batteries. *J. Electrochem. Soc.* **2021**, *168*, No. 030521.
(61) Chu, Y.; Xiong, S. Mixed transition-metal oxides@carbon core-shell nanostructures derived from heterometallic clusters for enhanced lithium storage. *Chin. Chem. Lett.* **2022**, *33*, 486−490.
(62) Mu, G.; Wu, B.; Ma, C.; Wu, F. Dynamics analysis of Si electrode particle size effect employing accurate Si model. *Electrochim. Acta* **2021**, *377*, No. 138110.
(63) Cao, W.; Han, K.; Chen, M.; Ye, H.; Sang, S. Particle size optimization enabled high initial coulombic efficiency and cycling stability of micro-sized porous Si anode via AlSi alloy powder etching. *Electrochim. Acta* **2019**, *320*, No. 134613.
(64) Iwamura, S.; Nishihara, H.; Kyotani, T. Fast and reversible lithium storage in a wrinkled structure formed from Si nanoparticles during lithiation/delithiation cycling. *J. Power Sources* **2013**, *222*, 400−409.
(65) Liu, W. R.; Guo, Z. Z.; Young, W. S.; Shieh, D. T.; Wu, H. C.; Yang, M. H.; Wu, N. L. Effect of electrode structure on performance of Si anode in Li-ion batteries: Si particle size and conductive additive. *J. Power Sources* **2005**, *140*, 139−144.
(66) Chu, Y.; Xi, B.; Xiong, S. One-step construction of MoO2 uniform nanoparticles on graphene with enhanced lithium storage. *Chin. Chem. Lett.* **2021**, *32*, 1983−1987.
(67) Cen, Y.; Qin, Q.; Sisson, R. D.; Liang, J. Effect of Particle Size and Surface Treatment on Si/Graphene Nanocomposite Lithium-Ion Battery Anodes. *Electrochim. Acta* **2017**, *251*, 690−698.
(68) Huang, W.; Wang, W.; Wang, Y.; Qu, Q.; Jin, C.; Zheng, H. Overcoming the fundamental challenge of PVDF binder use with silicon anodes with a super-molecular nano-layer. *J. Mater. Chem. A* **2021**, *9*, 1541−1551.

https://doi.org/10.1021/acsomega.3c01506
ACS Omega 2023, 8, 19772−19780